Met. Mater. Int., Vol. 19, No. 4 (2013), pp. 673~682
doi: 10.1007/s12540-013-4006-6

In Situ Fracture Observation and Fracture Toughness Analysis of Pearlitic Graphite Cast Irons with Different Nodularity

Seung Youb Han[1], Seok Su Sohn[1], Sang Yong Shin[1], Sunghak Lee[1,*], and Yong Chan Suh[2]

[1]Pohang University of Science and Technology, Center for Advanced Aerospace Materials, Pohang 790-784, Korea
[2]Hyundai Steel Co., Roll Technology, Department Pohang 790-370, Korea

(received date: 28 June 2012 / accepted date: 10 October 2012)

Effects of microstructural modification and microfracture mechanisms on fracture toughness of pearlitic graphite cast irons with different nodularity were investigated by *in situ* observation of microfracture process. Six pearlitic graphite cast irons were fabricated by adding a small amount of Mg as a nodularizing element for graphite, and their microstructures including pearlite, ferrite, graphite, and eutectic carbide were analyzed. Most of ferrites were observed in a layer shape around graphites because of carbon-depleted zones formed near graphites. As the nodularity and nodule count increased, fracture toughness linearly increased in the cast irons except the iron containing many fine graphites. According to *in situ* observation of microfracture process, cracks initiated at nodular graphites and carbides even at a small load, and then propagated readily through the adjacent graphites or carbides, thereby resulting in the lowest fracture toughness. The cast iron having widely spaced graphites and ferrite layers thickly formed around graphites showed the highest fracture toughness because of the blocking of crack propagation by ductile ferrite layers and the crack blunting and deflection by graphites, which was also confirmed by the R-curve analysis.

Key words: alloys, casting, In situ SEM, mechanical properties, fracture

1. INTRODUCTION

Fracture toughness is generally used for evaluating structural stability of materials, and is considered to be one of the most important material properties. Correlation studies of fracture toughness and microstructural characteristics, particularly the microfracture mechanism based on the microstructural control of each material concerned, are required to improve fracture toughness [1-5]. For example, pearlitic nodular cast irons used for core materials of work rolls can be fractured unexpectedly during hot rolling by fire cracking caused by thermal impact or thermal fatigue caused by the growth of internal cracks. This is generally resulted from the repeated formation of fire cracks or thermal-fatigue cracks and from the repeated impact load and the increased rolling load caused by abrupt intrusion of rolled plates [6-8]. It is also learned that pearlitic nodular cast irons consist of the pearlitic matrix, hard eutectic carbides, nodular graphites, and ferrites formed around graphites. Thus, analysis of microstructural factors determining fracture properties are critical in establishing overall rolling conditions, from which methods to improve the overall properties including fracture toughness should be suggested.

Since strengthening phases generally improve the strength of pearlitic graphite cast irons with different nodularity, while decreasing the fracture toughness, systematic understanding of the correlation between microstructural factors and mechanical properties is required for the accurate evaluation of fracture toughness, and microfracture mechanisms in relation with microstructural factors need to be elucidated. A simple way widely used to investigate microfracture mechanisms is a phenomenal observation of fractured surfaces, and microscopic observation of deformed microstructures beneath fractured surfaces have also been developed as effective experiments for fracture mechanism studies [9,10]. Despite of these research efforts, many difficulties still remain to be solved to correlate macroscopic fracture toughness with microscopic fracture mechanisms and to systematically analyze it.

The present study aims at presenting the effects of microstructural factors by investigating the correlation between microstructures and fracture toughness of pearlitic graphite cast iron with different nodularity and their microfracture mechanisms. For this purpose, six pearlitic graphite cast iron with different nodularity were fabricated by adding a small amount of Mg as nodularizing element for graphite, and

*Corresponding author: shlee@postech.ac.kr

their microstructures including various phases of pearlite, ferrite, graphites, and carbides were analyzed carefully. Mechanisms related with improvement of fracture toughness were examined by direct observation of microfracture processes using an *in situ* loading stage installed inside a scanning electron microscope (SEM) chamber. These experiments enabled to directly observe the crack initiation and propagation behavior occurring near a sharp notch tip and to study the R-curve behavior in which the fracture resistance increased with increasing crack growth.

2. EXPERIMENTAL PROCEDURES

2.1. Pearlitic graphite cast irons with different nodularity

The cast irons used in the present study were six pearlitic graphite cast irons where a small amount of Mg was added as nodularizing element for graphite, and their chemical compositions are shown in Table 1. The pouring temperature of graphites into the molten iron was 1340±15 °C. The nodularity (unit: %) and the nodule count (unit: ea·mm^{-2}) of graphites, which were varied in the range of 0-87% and 0-18 ea·mm^{-2}, respectively, were measured in accordance with the KS D 4302 standard specifications [11]. The nodule count was measured by counting the number of graphites whose shape factor was larger than 0.73 in five low-magnification (×100) optical micrographs at least. Here, when the area fractions of the graphite divided by the circular area whose diameter was the maximum length of the graphite were 0.51 or smaller, 0.51-0.65, 0.65-0.82, and 0.82 or larger, the shape factors were defined to be 0, 0.73, 0.92, and 1, respectively [11]. The nodularity of graphites was measured by the following equation:

$$\text{Nodularity (\%)} = \frac{0\times n_1 + 0.73\times n_2 + 0.92\times n_3 + 1\times n_4}{n_1+n_2+n_3+n_4} \quad (1)$$

where n_1, n_2, n_3, and n_4 were nodule count whose shape factors were 0, 0.73, 0.92, and 1, respectively. Smaller graphites than 20 μm were not counted in the measurement procedures of nodularity and nodule count. For convenience, pearlitic graphite cast iron with different nodularity and nodule count are referred to as 'G0N0', 'G60N6', 'G62N6', 'G65N6', 'G65N10', and 'G87N18'. For example, the 'G62N6' iron has the nodularity of 62% and the nodule count of 6 ea·mm^{-2}.

2.2. Microstructural analysis and tensile test

The alloys were polished, etched by a 2% nital solution, and observed by an optical microscope and an SEM (model; JSM-6330F, Jeol, Japan). Phases present in the irons were analyzed by energy dispersive spectroscopy (EDS), and their size and volume fraction were measured by an image analyzer (model: SigmaScan Pro, ver. 4.0, Jandel Scientific Co., CA).

Tensile specimens were obtained from the 1/2 thickness location of the cast iron ingots. Round tensile specimens having a gage length of 30 mm and a gage diameter of 6 mm were tested at room temperature at a strain rate of 2×10^{-4} s^{-1} by a universal testing machine (model; 5582, Instron, USA) of 100 kN capacity.

2.3. Fracture toughness test

The plane strain fracture toughness (K_{Ic}) was obtained by using a compact tension (CT) type specimen with a fatigued precrack. Because of the specimen thickness limit, J_{Ic} (plane strain value of J integral at the initiation of crack growth) was measured in accordance with the ASTM E1820 standard specifications [12], and then was converted to K_{Jc} by the following equation:

$$K_{Jc} = \sqrt{J_{Ic}\cdot E/(1-\nu^2)} \quad (2)$$

where E is elastic modulus. The measured K_{Jc} was used as a valuable K_{Ic} after checking if it met the ASTM requirement for minimum specimen dimensions [12]. The CT specimen whose dimensions were 25×25 mm with a thickness of 10 mm was used as shown in Fig. 1(a), and a fatigued precrack was introduced into this specimen. Fatigue precracking was done under a stress ratio, R, controlled within the range of $0.01<R<0.1$. All of the test values satisfy the ASTM requirement for minimum specimen dimensions of the ASTM E1820 specifications.

2.4. In situ SEM fracture test

A compact tension (CT) type loading stage was installed inside an SEM, on which a thin CT specimen with a thickness (grooved section) of 0.5 mm was placed to conduct the *in situ* SEM fracture test [13] (Fig. 1(b)). A sharp notch with a radius of 30-40 μm was inserted into the CT specimen by an electric discharge machine instead, considering the diffi-

Table 1. Chemical compositions of the pearlitic graphite cast iron with different nodularity (wt%)

Iron	Fe	C	Si	Cr	Mn	Ni	Mg	P+S
G0N0	Bal.	3.0±0.2	2.4±0.1	0.3±0.1	0.5±0.1	1.0±0.1	0.04±0.01	< 0.06
G60N6	Bal.	3.0±0.2	2.4±0.1	0.3±0.1	0.5±0.1	1.0±0.1	0.07±0.01	< 0.06
G62N6	Bal.	3.0±0.2	2.4±0.1	0.1±0.1	0.5±0.1	0.7±0.1	0.07±0.01	< 0.06
G65N6	Bal.	3.0±0.2	2.4±0.1	0.1±0.1	0.5±0.1	0.7±0.1	0.07±0.01	< 0.06
G65N10	Bal.	3.0±0.2	2.4±0.1	0.1±0.1	0.5±0.1	0.7±0.1	0.07±0.01	< 0.06
G87N18	Bal.	3.0±0.2	2.4±0.1	0.2±0.1	<0.1	1.3±0.2	0.07±0.01	< 0.06

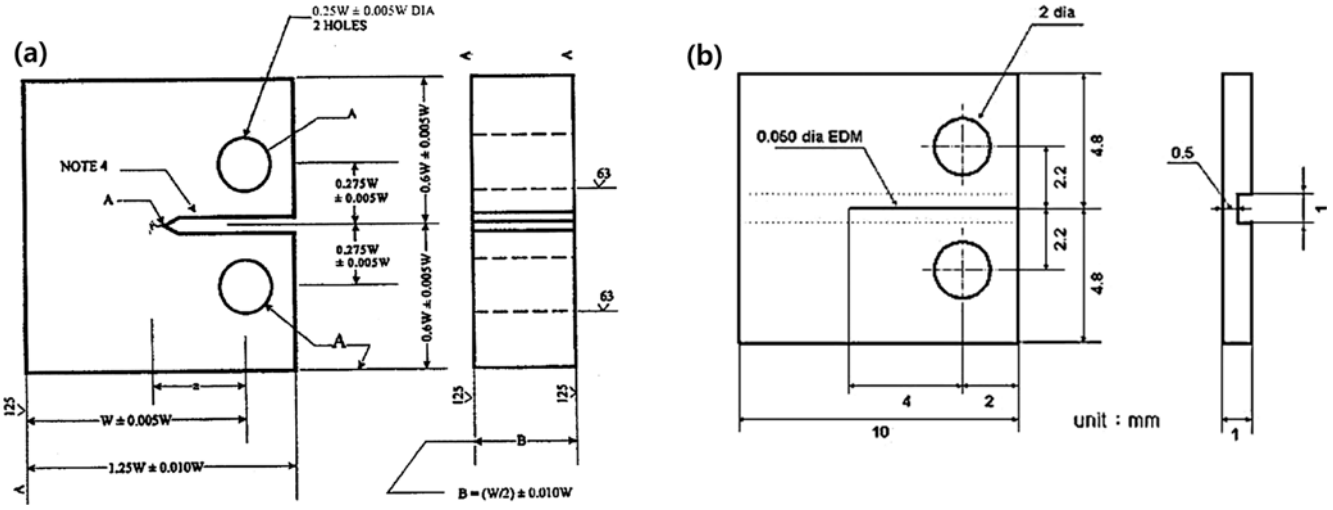

Fig. 1. The shape and dimensions of the (a) compact tension (CT) type specimen used for the K_{Ic} measurement, and (b) thin compact tension (CT) type specimen used for the *in situ* SEM fracture test (unit: mm).

culty to introduce a fatigue crack due to the brittle nature of the cast irons. The load applied to the specimen was continuously measured by a small-scale load cell (maximum load; 50 kg) installed in the stage. As the load was applied while observing and photographing the specimen surface displayed on an SEM screen, a crack was initiated and propagated at the notch tip at a certain stress intensity factor level. The stress intensity factor was measured at the photographing time of each SEM micrograph.

3. RESULTS

3.1. Microstructure

Figures 2(a) through (l) are optical micrographs of the six pearlitic graphite cast. Ferrites and pearlites are observed in a mixed form, and graphites, eutectic carbides, and ledeburites are found in all the irons except the G0N0 iron. The nodularity of graphite is varied from 0 to 87%, and their nodularity is highest in the G87N18 iron. Ledeburites are formed by a

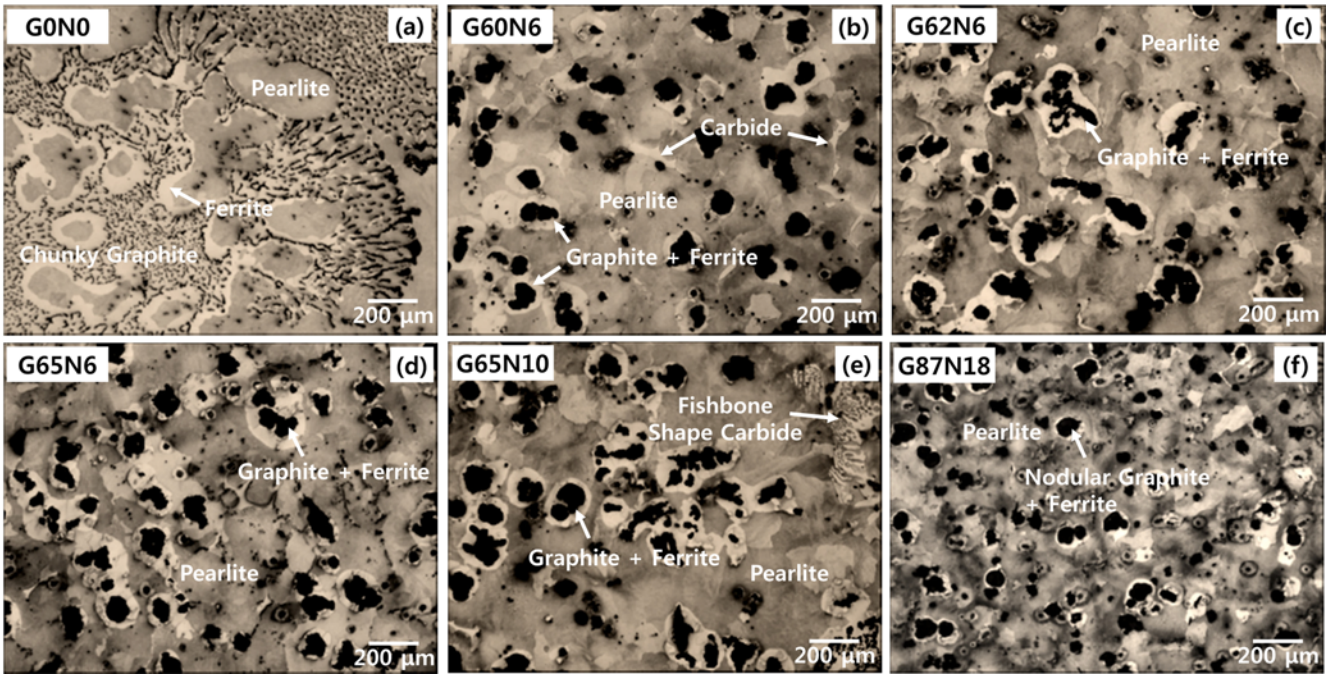

Fig. 2. Optical micrographs of the six pearlitic graphite cast irons : (a) and (g) G0N0, (b) and (h) G60N6, (c) and (i) G62N6, (d) and (j) G65N6, (e) and (k) G65N10, and (f) and (l) G87N18 irons.

Table 2. Quantitative analysis results of the pearlitic graphite cast iron with different nodularity

Iron	Volume Fraction (%)				Size of Graphites (μm)	Spacing of Graphites (μm)	Thickness of Ferrite Layer (μm)
	Pearlite	Ferrite	Graphite	Eutectic Carbide			
G0N0	79.5±8	18.2±5	–	2.3±1	–	–	–
G60N6	79.7±5	5.7±3	8.3±2	6.3±2	85±18	157±41	25±16
G62N6	71.5±4	15.9±5	9.5±3	3.1±2	88±25	144±47	29±19
G65N6	70.2±4	17.9±3	10.3±3	1.6±1	77±22	151±59	32±14
G65N10	73.3±5	14.8±4	10.5±4	1.4±1	78±31	134±61	28±19
G87N18	81.6±3	8.3±2	9.5±2	0.6±1	39±10	74±25	11±4

eutectic reaction of liquid → austenite (γ) + cementite (Fe_3C) at high temperatures, and then austenites are transformed into ferrites and pearlite during cooling [14-16]. In the present study, ledeburites are not classified because they are composed of ferrites, pearlites, and cementites. Most of ferrites exist in a layer form around graphites. In all the irons, volume fractions of ferrites, pearlites, graphites, and eutectic carbides, size and spacing of graphites, and thickness of ferrite layer surrounding graphites were measured, and the results are shown in Table 2.

In the G0N0 iron, graphites exist in a chunky form as they are not spheroidized (Fig. 2(a) and (g)). The volume fraction of ferrite is highest at about 18% among the six irons, and the volume fraction of carbide is 2.3%. In all the irons, the volume fraction of graphite is similar in the range of 8-10%, and the volume fraction of pearlite is higher than 70%, while the volume fractions of ferrite and carbide are different in each iron. In the G60N6 iron having nodularity of 60% and nodule count of 6 ea·mm^{-2}, the volume fraction of ferrite is lowest at about 6%, but the volume fraction of carbide is highest at about 6% (Figs. 2(b) and (h)). Though the G62N6 iron has the similar microstructure of the G60N6 iron, it has the higher volume fraction of ferrite and lower volume fraction of carbide (Figs. 2(c) and (i)). The G65N6 shows the highest nodularity (65%) among the irons having nodule count of 6 ea·mm^{-2}. It has the highest volume fraction of ferrite, while its volume fraction of carbide is 1.6% (Figs. 2(d) and (j)). In the G65N10 iron having same nodularity to the G65N6 iron, the volume fractions of ferrite and carbide are 15 and 1.4%, respectively (Figs. 2(e) and (k)). The G87N18 iron has the highest nodularity (87%) and nodule count (18 ea·mm^{-2}), and its volume fractions of ferrite and carbide are relatively low (Figs. 2(f) and (l)). With increasing nodule count, the size and spacing of graphites tend to decrease, as shown in Table 2. Most of graphites are found to be surrounded by ferrites as the C-depleted zones are formed near graphites. The thickness of ferrite layer ranges from 25 to 32 μm in all the irons except the G87N18 iron (11 μm). Most of carbides are formed inside the pearlite matrix between graphites, and some of them have fishbone shapes as indicated by arrows. According to the energy dispersive spectroscopy (EDS) data of eutectic carbides, excess iron and chromium are present in them, which suggests that they are chromium-rich iron carbides whose type might be M_3C, M_7C_3, or $M_{23}C_6$ [14-16].

Table 3. Tensile and fracture properties of the pearlitic graphite cast iron with different nodularity

Iron	Ultimate Tensile Strength (MPa)	Elongation (%)	Fracture Toughness (MPa·m$^{1/2}$)
G0N0	184±24	0.1±0.1	50±7
G60N6	232±12	0.2±0.1	58±3
G62N6	268±14	0.5±0.1	64±5
G65N6	307±10	1.4±0.2	67±3
G65N10	317±9	0.6±0.2	69±2
G87N18	356±7	0.7±0.1	40±2

The micro-Vickers-hardness values (load; 50 g) of pearlite, ferrite, graphite, and eutectic carbide are measured to be about 305, 131, 69, and 1340 VHN, respectively, and are similar in the six irons.

3.2. Tensile properties and fracture toughness

The room-temperature tensile data are summarized in Table 3. The ultimate tensile strength of the G0N0 iron without having nodular graphites is lowest at 184 MPa among the irons. As the nodularity and nodule count increase, the ultimate tensile strength almost linearly increases, while the tensile elongation tends to roughly increase. The increasing trend for elongation with increasing tensile strength is associated with the effect of the reduced stress concentration by graphites.

The fracture toughness of the six irons was measured using a CT type fracture toughness specimen with a fatigue precrack, and the data are shown in Table 3. The test data are average values obtained from two or more specimens. The fracture toughness of the G0N0 iron is relative low at 50 MPa·m$^{1/2}$. As the nodularity and nodule count increase, the fracture toughness linearly increases in the irons except the G87N18 iron. This shows the opposite to the previous results in which the fracture toughness increases with increasing nodularity and nodule count [17,18].

3.3. Observation of microfracture process

The *in situ* fracture initiation processes of the G87N18 iron containing fine graphites are shown in Figs. 3(a) through (h).

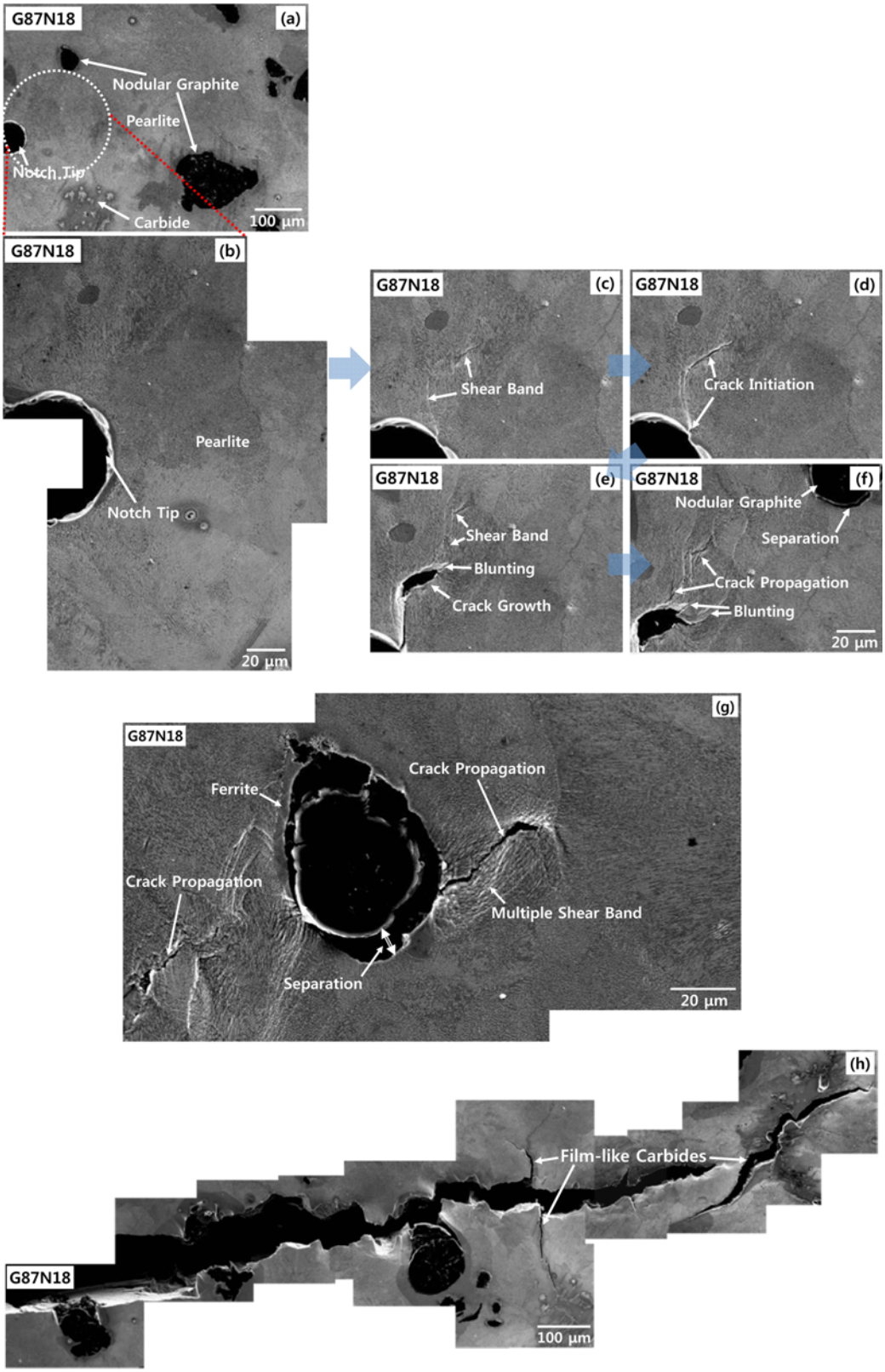

Fig. 3. A series of SEM micrographs near a notch tip of the G87N18 iron, showing (a) and (b) basic SEM microstructure, (c) and (d) shear band formation in the pearlite matrix near the notch tip (K_I = 41 MPa·m$^{1/2}$), (e) crack opening and blunting (K_I = 43 MPa·m$^{1/2}$), (f) crack propagation from the blunted crack (K_I = 49 MPa·m$^{1/2}$), (g) separation of graphite/matrix interface and crack propagation from the separated interface (K_I = 54 MPa·m$^{1/2}$), and (h) propagation path of the main crack (K_I > 60 MPa·m$^{1/2}$).

Figure 3(a) illustrates the low-magnification micrograph near the notch tip before loading, which contains fine nodular graphites and carbides in the pearlite matrix, as indicated by arrows. Figure 3(b) shows the magnified micrograph of the white dotted circle region of Fig. 3(a). When the load applied (stress intensity factor, $K_I = 41$ MPa·m$^{1/2}$), some shear bands are formed in the pearlite matrix near the notch tip, and a crack initiates at a deepened shear band (Figs. 3(c) and (d)). When the load increases ($K_I = 43$ MPa·m$^{1/2}$), the crack is opened and blunted, and other shear bands are formed in front of the blunted crack (Fig. 3(e)). At the increased stress intensity factor ($K_I = 49$ MPa·m$^{1/2}$), the crack propagates from the blunted crack, and more shear bands are formed in the pearlite matrix (Fig. 3(f)). A crack is also formed as an interface between graphite and matrix is separated as indicated by an arrow. In Fig. 3(g) ($K_I = 54$ MPa·m$^{1/2}$), the graphite/matrix interface is largely opened, and another crack propagates at this opened interface, near which a number of shear bands are well developed. The crack propagation path is shown in Fig. 3(h) ($K_I >$ 60 MPa·m$^{1/2}$). The overall crack propagation path has a relatively linear pattern, and the graphite/matrix interfacial separation and the cracking of nodular graphites are frequently observed. In the crack path, carbides are cracked, but it is not likely that these cracks affect the deflection of crack path.

Figures 4(a) through (g) provide a series of SEM micrographs showing the microfracture process near a notch tip of the G65N10 iron. As the load is applied at a relatively high stress intensity level ($K_I = 70$ MPa·m$^{1/2}$), a crack initiates at the notch tip (Fig. 4(a)). Graphites, carbides, ferrites, and pearlites are indicated by arrows. When the stress intensity factor increases to 78 MPa·m$^{1/2}$, most of carbides located near the notch tip are cracked, and some of them are connected to form a long crack (Fig. 4(b)). Figures 4(c) through (e) show the propagation process of the cracks initiated at carbides. These cracks are connected to other cracks initiated at carbides and graphite/matrix interfaces under the increased stress intensity (Fig. 4(d), $K_I = 81$ MPa·m$^{1/2}$). They are largely opened, and then are connected with the crack initiated at the notch tip (Fig. 4(e)). When the stress intensity factor increases to 88 MPa·m$^{1/2}$, the main crack initiated from the notch tip propagates to a graphite, and the graphite/matrix is opened (Fig. 4(f)). Here, the ferrite is deformed to induce the crack blunting. At the stress intensity factor of 90 MPa·m$^{1/2}$, the main crack propagates to another graphite, where the ferrite/graphite interfacial separation and crack blunting at the ferrite occur simultaneously to further raise the stress intensity factor (Fig. 4(g)).

4. DISCUSSION

The fracture mechanism of the pearlitic graphite cast iron with different nodularity is quite complicated because a number of microstructural features play an important role in the fracture process. These features can be classified generally into the following two categories; 1) distribution of graphites and carbides, *e.g.*, type, size, shape, and volume fraction, and 2) features governing matrix properties, *e.g.*, pearlitic matrix phase. Due to the large amount of graphites and carbides, the pearlitic graphite cast irons have excellent hardness and strength. According to the *in situ* examination of the fracture process, however, cracks initiate at these graphites and carbides even at a small load, and then propagate readily through the adjacent graphites or carbides, thereby resulting in the low fracture toughness levels of the cast irons. In order to improve fracture toughness of the pearlitic graphite cast iron, thus, the amount, size, spacing, and distribution of graphites and carbides as well as the matrix phase that would control to restrain the crack propagation should be considered carefully.

Pearlitic graphite cast irons with different nodularity fabricated in the present study contain alloying elements of Mn, Cr, Ni, and Mg as well as basic elements of C, Si, P, and S, as shown in Table 1. Mn accelerates the carbide formation and retards the ferrite formation [19-22]. Cr forms relatively coarse carbides, and raises the carbide formability when a sufficient amount of Mn coexists. Ni, as an austenite stabilizer, lowers the austenite-graphite processing temperatures, and restrains the formation of ferrite. It also plays a role in preventing the formation of coarse carbides by decreasing meta-stable austenite-carbide reaction temperatures. Mg works as an important element for forming nodular graphites [19-21]. It forms Mg-containing complex oxides or sulfides by acting as inoculants inside a molten iron pool, while it strongly works for deoxidization and desulfurization. In the G0N0 iron, chunky graphites are formed instead of nodular graphites because of the low containment (0.04 wt%) of Mg (Tables 1 and 2). Other irons except the G0N0 iron, show the nodularity of 60% or higher as they contain a sufficient amount of Mg (0.07 wt%). The G87N18 iron containing 1.3 wt% of Ni has the highest nodularity and nodule count. The G60N6, G62N6, G65N6, and G65N10 irons have the similar nodularity and nodule count as their compositions are not varied much.

According to the *in situ* fracture observations of the G87N18 iron containing many fine nodular graphites, initial microcracks are formed mainly at the pearlite matrix by forming shear bands as can be seen in Figs. 3(c) and (d). They propagate mainly along deepened shear bands to develop into a long crack and to connect with a microcrack formed by the graphite/matrix interfacial separation (Figs. 3(d) through (f)). These nodular graphites are relatively closely spaced in the pearlite matrix, and are susceptive to graphite/matrix interfacial separation because of their weakness of interfaces. These graphite/matrix interfaces are readily separated at a relatively low stress intensity factor level to develop microcracks, and are connected with cracks propagated along the pearlite matrix

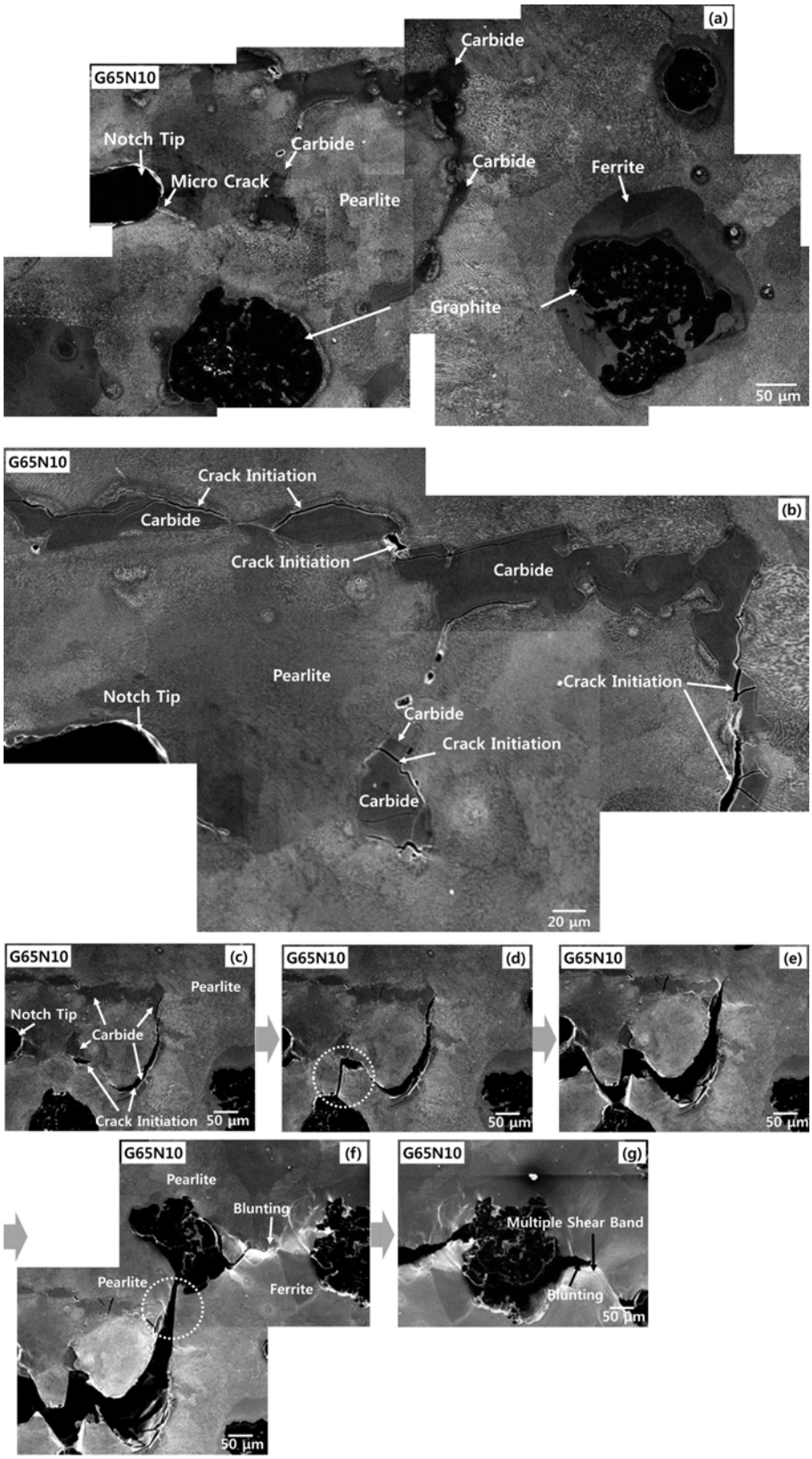

Fig. 4. A series of SEM micrographs near a notch tip of the G65N10 iron, showing (a) crack initiation at the notch tip (K_I = 70 MPa·m$^{1/2}$), (c) cracking of carbides located near the notch tip (K_I = 78 MPa·m$^{1/2}$), (d) crack propagation to other cracks initiated at carbides and graphite/matrix interfaces (K_I = 81 MPa·m$^{1/2}$), (e) crack connection with the crack initiated at the notch tip (K_I = 85 MPa·m$^{1/2}$), (f) main crack propagation to a graphite and crack blunting in front of a ferrite layer (K_I = 88 MPa·m$^{1/2}$), and (g) the main crack propagation to another graphite (K_I = 90 MPa·m$^{1/2}$).

[9,10]. In the crack propagation path (Fig. 3(g)), the graphite/matrix interfacial separation is frequently observed, and the pearlite matrix provides the easy crack propagation path, thereby resulting in the low fracture toughness (Table 3).

In the G65N10 iron containing coarse graphites, on the other hand, graphites are more widely spaced than in the G87N18 iron (Table 2). These graphites work as brittle fracture initiation sites deteriorating fracture toughness because graphite/matrix interfaces are separated to form microcracks, but these interfaces are largely opened and connected to form a zig-zag bent crack under a relatively high stress intensity (Figs. 4(c) through (f)). Widely spaced graphites give more chances for crack opening and blunting and for crooked crack propagation path, which can induce the deflection of cracks and favorably affect the fracture toughness. In addition, ferrite layers surrounding graphites play an important role in blocking the crack propagation because ferrite layers have ductile characteristics than the pearlite matrix. The presence of ferrite layers around graphites can restrain the crack propagation and thereby induce the ductile fracture by the formation of shear bands in the ligaments between the pearlite matrix and graphites as shown in Figs. 4(f) and (g), which can lead to the additional improvement of fracture toughness. Thus, the G65N10 iron has much better fracture toughness than G87N18 iron. The G87N18 iron contains thin ferrite layers as they are thinly formed at C-depleted zones around fine nodular graphites. This acts as a reason why the pearlitic matrix allows the abrupt crack propagation with little plastic deformation (Fig. 3(g)). The effect of the matrix phase on the obstruction process of crack propagation is not sufficient in the G87N18 iron.

Figures 5(a) and (b) show the correlation between the volume fraction and thickness of ferrite layers and fracture toughness in the five irons. The G0N0 iron is excluded because it does not contain nodular graphites. As the volume fraction increases, the fracture toughness increases, although the G87N18 iron shows considerably low fracture toughness (Fig. 5(a)). The linear proportional relation between the thickness of ferrite layer and fracture toughness is more clearly visible in Fig. 5(b). It is clear from the *in situ* fracture observation that the superior fracture toughness in the G65N10 iron is attributed to the role of ferrite layer in restraining the crack propagation. When a propagating crack encounters the matrix, the ferrite phase can serve as an obstacle to the crack propagation, whereas the pearlitic phase offers the lesser resistance to crack propagation than the ferrite phase does. Since the crack propagation through the relatively ductile ferrite phase is somewhat difficult in such case, the crack propagates mostly along a tortuous fracture path, thereby leading to the enhancement of fracture toughness.

In addition to the importance of the presence of ferrite layer, the existence of carbides should be considered. A considerable amount of carbides are present in the pearlitic matrix, and negatively affect the fracture processes because of their hardness (1340 VHN) and brittleness. As shown in the *in situ* fracture observation results (Figs. 4(b) through (e)), carbides are readily cracked, and provides the propagation path of cracks. Figure 5(c) shows the correlation between the volume fraction of carbides formed in the pearlite matrix and fracture toughness. The fracture toughness tends to decrease with increasing volume fraction of carbides is observable, although the G87N18 iron shows the opposite trend. In the G87N18 iron, the thin ferrite layer and small spacing between nodular graphites seem to more negatively affect the fracture toughness than the volume fraction of carbides. However, it is likely that carbides do not affect much the deterioration of fracture toughness because some of them help to induce the deflection of cracks which is favorable for the resistance to crack propagation and can considerably compensate the negative effect of carbides (Figs. 4(c) through (e)).

The G65N10 iron shows a stable crack growth as shown in Figs. 4(c) through (g), which indicates the higher resistance to crack growth than that of the G87N18 iron. Figure 6 shows R-curves of the G65N10 and G87N18 irons obtained by plotting both crack propagation length and stress intensity factor measured during the *in situ* fracture test. In the G65N10 iron, the crack initiates at a relatively high stress intensity factor level, and stably propagates to reach the fracture. The stress intensity factor at the time of crack initiation, *i.e.,* apparent fracture toughness, of the G65N10 iron is 70 MPa·m$^{1/2}$, which

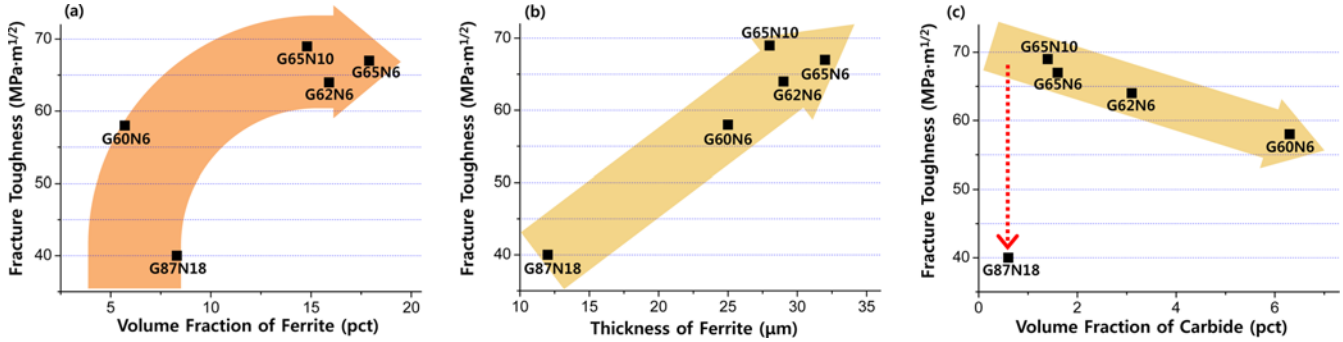

Fig. 5. Fracture toughness *vs* (a) volume fraction of ferrite, (b) thickness of ferrite layer, and (c) volume fraction of eutectic carbide.

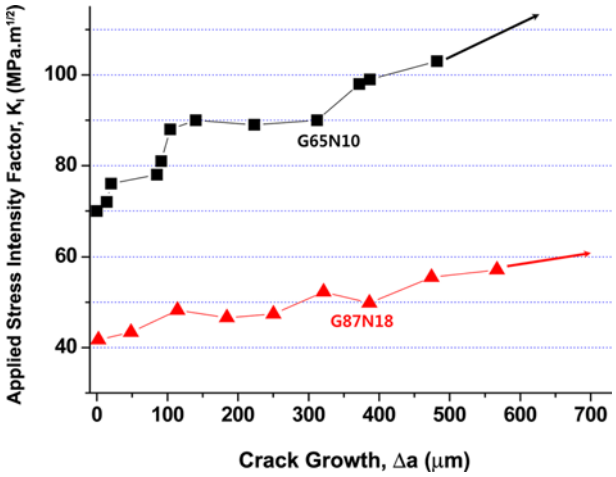

Fig. 6. Fracture resistance curves (R-curves) of the G65N10 and G87N18 irons.

is slightly higher than the measured fracture toughness (Table 3), and steadily increases with increasing crack length, finally reaching up to 100 MPa·m$^{1/2}$ or higher and showing the R-curve behavior. This increase in the resistance to crack growth of the G65N10 iron is associated with a large amount of crack deflection as ductile ferrite layers effectively blocks the crack propagation and some carbides help to induce the crack deflection. As a result of the occurrence of crack blunting at the blocked sites of the predominant crack, the higher stress intensity factor is required for the further crack propagation as seen in Figs. 4(e) through (g). This R-curve of the G65N10 iron shows the increasing resistance to crack growth according to the crack blunting and deflection.

The R-curve behavior also occurs in the G87N18 iron, like in the G65N10 iron, as the crack propagation is often blocked by the graphite/matrix interfacial separation and shear band formation in the pearlite matrix. However, the R-curve effect of the G87N18 iron is much weaker than that of G65N10 iron, and the apparent fracture toughness of the G87N18 iron (42 MPa·m$^{1/2}$) is much lower than that of the G65N10 iron, which is well matched with the fracture toughness data of Table 3.

Since the *in situ* fracture test is a good method to directly observe the effects of microstructural factors such as graphites, ferrite layers, eutectic carbides, pearlite matrix on microfracture behavior, it can be effectively used to analyze the fracture behavior of pearlitic graphite cast iron with different nodularity. The present study confirms enhanced fracture properties of the G65N10 iron over the G87N18 iron according to the R-curve behavior. This effect is explained by mechanisms of (1) blocking of crack growth and (2) crack blunting and deflection. The G65N10 iron has the high strength owing to the increase in volume fraction of hard pearlite phase, and has the best fracture toughness owing to the crack blunting and deflection by widely spaced graphites and ferrite layers thickly formed around graphites. This improvement of mechanical and fracture properties opens new possibilities for its proper application to pearlitic graphite cast irons requiring excellent mechanical and fracture properties simultaneously because the appropriate nodularity of graphites and nodule count are effective for the microstructural modification and property improvement. Efforts are needed in the future to establish appropriate processing variables, to analyze the microstructural factors in association with fracture mechanisms, and the design of the matrix alloy composition, in light of economic considerations.

5. CONCLUSIONS

Effects of microstructural modification and microfracture mechanisms on fracture toughness of pearlitic graphite cast iron with different nodularity were investigated by *in situ* observation of microfracture process.

(1) The fracture toughness of the G0N0 iron where graphites were not spheroidized was relative low. As the nodularity and nodule count increased, the fracture toughness linearly increased in the irons except the G87N18 iron because the G87N18 iron had the lowest toughness in spite of its highest nodularity and nodule count.

(2) In the G87N18 iron, the thin ferrite layer and small spacing between nodular graphites negatively affected the fracture toughness. According to *in situ* observation of microfracture process, cracks initiated at nodular graphites and carbides even at a small load, and then propagated readily through the adjacent graphites or carbides, thereby resulting in the lowest fracture toughness.

(3) The G65N10 iron had the highest fracture toughness owing to widely spaced graphites and ferrite layers thickly formed around graphites, while it had the high strength owing to the increase in volume fraction of pearlite matrix. This highest fracture toughness was associated with a large amount of crack deflection as ductile ferrite layers effectively blocked the crack propagation.

REFERENCES

1. N. Bonora and A. Ruggiero, *Int. J. Solids Struct.* **42**, 1401 (2005).
2. K.-P. Jen, J. T. Scardina, and D. G. Smith, *Eng. Fract. Mech.* **22**, 227 (1985).
3. P. P. Rao and S. K. Putatunda, *Mater. Sci. Eng. A* **349**, 136 (2003).
4. S. Kim, S. Lee, K. Han, S. Hong, and C. Lee, *Met. Mater. Int.* **16**, 483 (2010).
5. J. H. Yoon, S. H. Kang, Y. Lee, and S. S. Kim, *Korean J. Met. Mater.* **50**, 8 (2012).
6. S. J. Manganello, *Rolls for the Metal Working Industries* (eds. R. B. Corbett), p.227, Iron and Steel Society, Warren-

dale, PA (1990).
7. C.-H. Lim and B.-C. Goo, *Met. Mater. Int.* **17**, 199 (2011).
8. S. Lee, D. H. Kim, J. H. Ryu, and K. Shin, *Metall. Mater. Trans. A* **28**, 2595 (1997).
9. F. Iacoviello, O. D. Bartolomeo, V. D. Cocco, and V. Piacente, *Mater. Sci. Eng. A* **478**, 181 (2008).
10. M. J. Dong, C. Prioul, and D. Francois, *Metall. Mater. Trans. A* **28**, 2245 (1997).
11. KS D 4302, *Spheroidal Graphite Iron Casting*, Korea Standard Association (2001).
12. ASTM Standard E1820-09, *Standard Test Measurement of Fracture Toughness*, ASTM (2009).
13. K.-S. Sohn, K. Euh, S. Lee, and I. Park, *Metall. Mater. Trans. A* **29**, 2543 (1998).
14. P. Chaengkham and P. Srichandr, *J. Mater. Process. Technol.* **211**, 1372 (2011).
15. C. K. Kim, J. I. Park, S. Lee, Y. C. Kim, N. J. Kim, and J. S. Yang, *Metall. Mater. Trans. A* **36**, 87 (2005).
16. E.-J. Chun, J.-S. Lee, H. Do, S.-J. Kim, Y.-S. Choi, Y.-H. Park, and N. Kang, *Korean J. Met. Mater.* **50**, 487 (2012).
17. R. Salzbrenner, *J. Mater. Sci.* **22**, 2135 (1987).
18. R. K. Dasgupta, D. K. Mondal, A. K.Chakrabarti, and A. C. Ganguli, *J. Mater. Eng. Perform.* **21**, 1728 (2012).
19. W. F. Smith, *Structure and Properties of Engineering Alloys*, *2nd ed.*, pp.335-384, McGraw-Hill Book Co., New York (1993).
20. M. Martínez-Madrid, M. A. Acosta, A. Torres-Acosta, R. Rodríguez-T, and V. M. Castaño, *J. Mater. Eng. Perform.* **11**, 651 (2002).
21. C. H. Hsu and T. L. Chuang, *Metall. Mater. Trans. A* **32**, 2509 (2001).
22. C. Y. Kang and T. Y. Hur, *Korean J. Met. Mater.* **50**, 413 (2012).